

# Deep, Deep Learning with BART

Moritz Blumenthal<sup>1</sup>, Guanxiong Luo<sup>1</sup>, Martin Schilling<sup>1</sup>, H. Christian M. Holme<sup>1,3</sup>,  
and Martin Uecker<sup>\*1,2,3,4</sup>

<sup>1</sup>Institute for Diagnostic and Interventional Radiology, University Medical Center Göttingen,  
Göttingen, Germany

<sup>2</sup>Institute of Biomedical Imaging, Graz University of Technology, Graz, Austria

<sup>3</sup>German Centre for Cardiovascular Research (DZHK), Partner Site Göttingen, Göttingen, Germany

<sup>4</sup>Cluster of Excellence “Multiscale Bioimaging: from Molecular Machines to Networks of Excitable Cells” (MBExC), University of Göttingen, Germany

March 1, 2022

## Abstract

**Purpose:** To develop a deep-learning-based image reconstruction framework for reproducible research in MRI.

**Methods:** The BART toolbox offers a rich set of implementations of calibration and reconstruction algorithms for parallel imaging and compressed sensing. In this work, BART was extended by a non-linear operator framework that provides automatic differentiation to allow computation of gradients. Existing MRI-specific operators of BART, such as the non-uniform fast Fourier transform, are directly integrated into this framework and are complemented by common building blocks used in neural networks. To evaluate the use of the framework for advanced deep-learning-based reconstruction, two state-of-the-art unrolled reconstruction networks, namely the Variational Network [1] and MoDL [2], were implemented.

**Results:** State-of-the-art deep image-reconstruction networks can be constructed and trained using BART’s gradient based optimization algorithms. The BART implementation achieves a similar performance in terms of training time and reconstruction quality compared to the original implementations based on TensorFlow.

**Conclusion:** By integrating non-linear operators and neural networks into BART, we provide a general framework for deep-learning-based reconstruction in MRI.

**Keywords:** MRI, image reconstruction, inverse problems, deep learning, parallel imaging, automatic differentiation

Submitted to Magnetic Resonance in Medicine

---

\*Graz University of Technology, Institute of Biomedical Imaging, Stremayrgasse 16/3, 8010 Graz, AUSTRIA uecker@tugraz.at

# 1 Introduction

In the last decades, magnetic resonance imaging (MRI) has advanced substantially in terms of acquisition speed and image quality. Parallel imaging utilizes the signal of multiple receiver coils for image reconstruction by combining the signals in k-space [3, 4, 5] or image space [6]. Another step towards the current state-of-the-art image reconstruction was the use of compressed sensing for MRI [7, 8]. Advanced methods now integrate compressed sensing and parallel imaging by using sparsifying regularization terms when solving the inverse problem for parallel imaging [8, 9]. These techniques admit a Bayesian interpretation where regularization terms can be understood as the integration of prior knowledge into the reconstruction.

In recent years, deep learning has become a major research interest in image reconstruction with the goal to improve upon the previously used hand-crafted regularization terms by learning image properties from large data sets. The public availability of deep learning frameworks such as TensorFlow [10] or PyTorch [11] simplifies access to deep learning methods for MRI researchers. Moreover, public data sets from `mridata.org` [12, 13] and from the fastMRI challenge [14] provide a large amount of training data and open the field of research to data scientists not having access to MRI data.

Neural networks have been utilized in various ways for MRI reconstruction. Some authors have proposed to learn a direct mapping from the acquired k-space data to the image domain [15]. However, these methods usually lack a data-consistency guarantee, i.e. the output of the reconstruction may not be consistent with the measured k-space data. Others have used neural network to train regularizers which can be used for image reconstruction in a subsequent step [16]. In one class of such regularizers, a neural network is trained to enhance an initial reconstruction. Afterwards, the  $\ell_2$  difference to this reconstruction is used as regularizer [17, 18]. Another class of networks with data consistency are networks that model an unrolled iterative optimization algorithm [1, 2, 19]. In each iteration of such a network, the network part, usually a CNN or U-Net, updates the current reconstruction and afterwards soft data consistency is imposed by a gradient step or proximal mapping. The resulting unrolled networks are then trained as an end-to-end mapping from the k-space to the image domain.

BART [20] is an open-source framework providing implementations of various calibration methods and reconstruction algorithms for parallel imaging and compressed sensing. It consists of programming libraries and command line tools for easy but flexible access to the programming libraries. BART is developed with the purpose of facilitating reproducible research and has a focus on backwards compatibility, while still offering rapid prototyping and testing of advanced reconstruction algorithm with the goal of translating them into clinical reconstruction pipelines. The high-level reconstruction algorithms of BART are built around programming libraries offering generic implementations of various iterative algorithms as well as an efficient numerical backend. The backend provides functions acting on multidimensional arrays (or tensors) which support acceleration by multiple threads or (multiple) graphical processing units (GPUs). In this work, we extend BART with a complete framework for non-linear operators. The framework builds on our previous work on non-linear calibrationless parallel imaging [21] and physics-based reconstruction [22], and is now extended with automatic differentiation, additional building blocks for neural networks, and new optimization algorithms [23]. In combination with the powerful numerical backend, the non-linear operator framework can then be used to efficiently train neural networks. Moreover, non-linear opera-

tors can be used to wrap around TensorFlow graphs, allowing the integration of pre-trained networks into BART’s reconstruction algorithms [24]. MRI reconstruction networks imposing data consistency require a large amount of domain specific knowledge. By integrating neural networks into BART, we benefit from BART’s rich set of MRI specific modules and algorithms which can be easily reused for deep learning based MRI reconstructions. Written in C and only depending on a few external libraries, we consider BART a solid basis for future research that integrates classical image reconstruction with deep learning.

In the remainder of this manuscript we first describe in detail the implementation of our deep learning framework and its integration into BART. There, we focus on the numerical backend, the automatic differentiation, the iterative training algorithms and the neural network framework. Afterwards, we present our implementation of the Variational Network (VarNet)[1] and MoDL [2], and compare their performance to the original implementations based on TensorFlow.

## 2 Methods

A neural network is a non-linear function  $F$  mapping the input data  $\mathbf{x}$  and weights  $\theta$  to an output  $\mathbf{y} = F(\mathbf{x}; \theta)$ . Training a neural network corresponds to fitting the neural network to a training dataset by minimizing some suitable loss  $L$ , i.e.

$$\theta^* = \arg \min_{\theta} \left[ \sum_i L(\mathbf{y}_i, F(\mathbf{x}_i; \theta)) \right]. \quad (1)$$

Usually, neural networks are constructed from small building blocks such as fully-connected layers, convolutional layers or activation functions. Automatic differentiation is used to compute the gradients of the loss needed for gradient-based optimization algorithms such as stochastic gradient descent or ADAM [25]. Offering automatic differentiation and efficient implementations for the small building blocks are the key features of deep learning frameworks. In the first part of this section, we describe the integration of programming libraries used for deep learning in BART, before we describe our implementations of VarNet and MoDL in the second part.

### 2.1 Libraries for Deep Learning in BART

The basic integration of libraries used for neural networks in BART is depicted in Figure 1. The backend provide access to optimized numerical functions. Based on the backend, the non-linear operator framework is used to construct neural networks from small building blocks and provides automatic differentiation to compute gradients. The nn-library then extends this non-linear operator framework by deep learning specific functions. Finally, new training algorithms for deep learning are integrated in BART’s iterative framework.

#### 2.1.1 Numerical Backend

The numerical backend of BART is designed around functions acting on multidimensional (md) arrays. An md-array is described by its dimensions  $\mathbf{d} \in \mathbb{N}^N$ , its rank  $N$  and, optionally, its strides  $\mathbf{s} \in \mathbb{Z}^N$  describing how an element of the md-array is accessed in memory. The

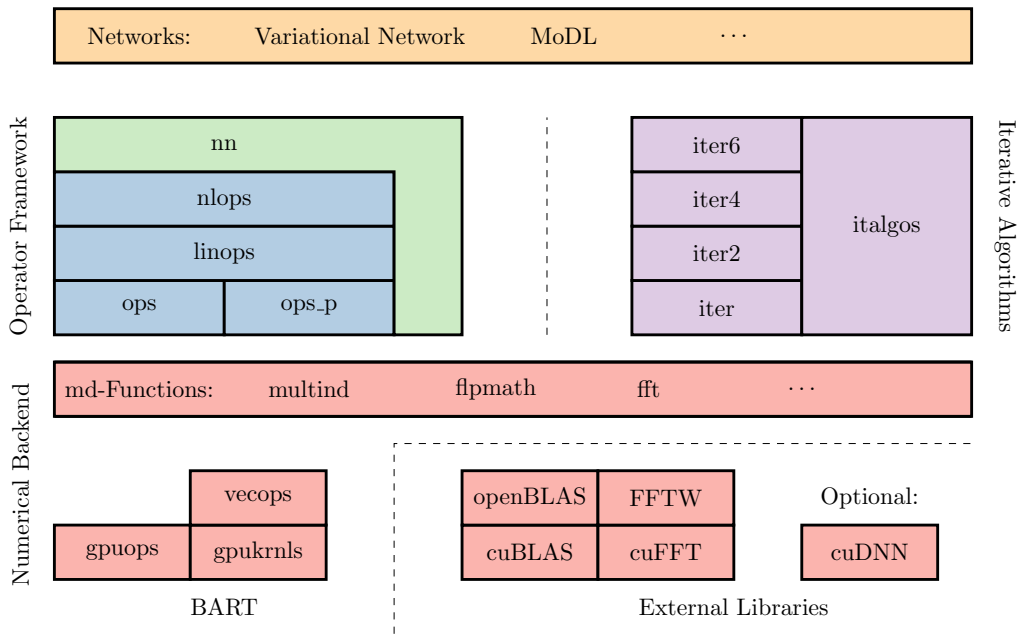


**Figure 1:** Integration of deep learning modules into BART. The numerical backend (red) is accessed by md-functions which invoke BART’s internal generically-optimized functions or external libraries offering highly optimized code for special functions. Differentiable neural networks are implemented as non-linear operators (blue). The nn-library (green) extends the non-linear operator framework by deep learning specific features. The training algorithms are integrated in BART’s iterative framework (violet). Iter6 provides a new interface for batched gradient-based training algorithms.

offset of an element at position  $\mathbf{p} \in \mathbb{N}^N$  is given by  $o = \mathbf{p} \cdot \mathbf{s}$ . By default, BART assumes column-major ordering, i.e. the first dimension of the md-array is stored continuously in memory corresponding to the strides  $\mathbf{s}_i = \prod_{j=0}^{i-1} \mathbf{d}_j$ . By manipulating the strides, different views on the memory can be generated without copying data. The memory for an md-array can be allocated on the CPU or on the GPU. On supported GPUs, the GPU memory can be oversubscribed, i.e. GPU memory is automatically swapped by the driver to CPU memory.

**Md-Functions** To perform computations on md-arrays, BART provides a consistent and flexible interface to the numerical backend, the so-called md-functions. Md-functions usually loop over all positions defined by the dimensions and apply a scalar-valued kernel on the elements accessed using the provided strides. For example, the `md_fmacc2` function takes the dimensions  $\mathbf{d}$ , pointers to the arrays  $a$ ,  $b$  and  $c$  and strides  $\mathbf{s}^x$  for all three arrays. It applies

$$\begin{aligned} \text{for } \mathbf{p} \in \{0, \dots, \mathbf{d}_0 - 1\} \times \dots \times \{0, \dots, \mathbf{d}_{N-1} - 1\} : \\ a[\mathbf{p} \cdot \mathbf{s}^a] \leftarrow a[\mathbf{p} \cdot \mathbf{s}^a] + b[\mathbf{p} \cdot \mathbf{s}^b] \cdot c[\mathbf{p} \cdot \mathbf{s}^c] \end{aligned} \quad (2)$$

If the strides correspond to the default column-major ordering strides, the function acts pointwise, however, by manipulating the strides, many functions can be expressed by the `md_fmacc2`. For example, by setting  $\mathbf{p}^a = 0$  always the same element  $a[0]$  is accessed in which the product of  $b$  and  $c$  is accumulated, corresponding to a dot product of  $b$  and  $c$ . Similarly, a strided call to `md_fmacc2` can be used to compute a matrix-vector product, matrix-matrix product or a valid-type convolution.

While md-functions provide a unified interface to the numerical backend, the actual executed code is optimized automatically in the backend. If the arrays are located on the GPU, the corresponding GPU code is executed providing transparent GPU acceleration. On the CPU, the code is parallelized automatically to multiple threads if possible. For specific combinations where BART’s generic optimization is not sufficient, specialized code is called. For example, matrix-matrix multiplications are outsourced to external BLAS libraries. Similarly, cuDNN can be used to compute convolutions, however, we have also implemented convolutions directly in BART to have as few required dependencies as possible.

**Bitwise Reproducibility** Floating point arithmetic is not associative making multi-threaded programs non-deterministic if the order of the operations depends on the runtime of individual threads. BART’s GPU kernels and the generic parallelization do not introduce any non-deterministic operations except for the gridding code of the nuFFT. cuBLAS and cuDNN are deterministic across runs when executed on GPUs with the same architecture except for some specific functions. By default, BART makes only use of these deterministic functions, however, the compile-time option `NON_DETERMINISTIC=1` can be used to allow BART to select non-deterministic algorithms to improve computational performance.

### 2.1.2 Automatic Differentiation and the Non-Linear Operator Framework

In BART, neural networks are represented by non-linear operators (`nlops`). These allow construction of complicated functions from small building blocks and computation of the derivatives of these functions. An `nlop` consists of the non-linear forward operator  $F$  having

$I$  inputs  $\mathbf{x}_i$  and  $O$  outputs  $\mathbf{y}_o = F_o(\mathbf{x}_1, \dots, \mathbf{x}_I)$  and the derivatives  $D_i F_o$  for each combination of inputs and outputs, i.e.

$$F : \mathbb{C}^{N_1 + \dots + N_I} \rightarrow \mathbb{C}^{M_1 + \dots + M_O} \quad D_i F_o : \mathbb{C}^{N_i} \rightarrow \mathbb{C}^{M_o}$$

$$[\mathbf{x}_1, \dots, \mathbf{x}_I] \mapsto [\mathbf{y}_1, \dots, \mathbf{y}_O] \quad d\mathbf{x}_i \mapsto d\mathbf{y}_o = \left( \frac{\partial \mathbf{y}_o}{\partial \mathbf{x}_i} \Big|_{(\mathbf{x}_1, \dots, \mathbf{x}_I)} \right) d\mathbf{x}_i. \quad (3)$$

The derivatives are linear operators applying the Jacobian matrix on their inputs. The Jacobian matrix is always evaluated at the last input of the non-linear forward operator  $F$ . For operators  $F$  which are not holomorphic, i.e. no derivative with respect to the complex numbers exists, we interpret the real and imaginary channel independently and compute derivatives over the real numbers. As all linear operators in BART, the derivatives can also be used to apply the adjoint derivative  $D_i F_o^H$ , which is exploited to compute gradients of  $F$ . In the special case that  $F : \mathbb{C}^N \rightarrow \mathbb{R}$  maps to a scalar, the Jacobian matrix reduces to the gradient of  $F$  which can be computed by applying the adjoint derivative on a 1, i.e.

$$\left( \frac{\partial \text{Re}[F]}{\partial \text{Re}[x_1]}, \frac{\partial \text{Re}[F]}{\partial \text{Im}[x_1]}, \dots, \frac{\partial \text{Re}[F]}{\partial \text{Re}[x_N]}, \frac{\partial \text{Re}[F]}{\partial \text{Im}[x_N]} \right)^T = \left( \frac{\partial F}{\partial \mathbf{x}} \right)^H = D F^H \mathbf{1}. \quad (4)$$

If  $F$  itself is composed of multiple `nlops`, applying the adjoint derivative corresponds to the well-known backpropagation algorithm.

The inputs and outputs of forward operator and the derivatives are md-arrays which can be located on the CPU or the GPU. The application of the respective operators is implemented based on md-functions such that the computation of the whole operators is automatically outsourced to the GPU if the inputs and outputs are located on the GPU.

**Implementation of operators** This paragraph describes the implementation details of `nlops` in BART. In addition to `nlops`, BART implements two other classes of operators, i.e. `linops` modeling linear operators and `plain operators`. While `operators` are used for the actual application and composition of operators, `nlops` and `linops` are structures combining several `operators` to provide a high level interpretation.

The basic structure of atomic, i.e. non-composed, `operator` is depicted in Figure 2A. An `operator` holds a reference to a data structure `data` and a function `apply` which is called when the operator is applied. The data structure can for example hold a matrix, if the operator is used to multiply an input vector with a matrix. When the `operator` is applied, the `apply` function is passed references to pre-allocated memory for the inputs and outputs and the data structure of the operator.

A `linop`  $A : \mathbb{C}^N \rightarrow \mathbb{C}^M$  models a linear operator. `linops` can be used to apply the linear operator  $A$  and its adjoint  $A^H$ , where both,  $A$  and  $A^H$ , are implemented as independent `operators`. Moreover, a `linop` can contain an `operator` for an optimized implementation of the chained forward and adjoint operator  $A^H A$  or its regularized inverse. The four `operators` of an atomic `linop` have access to a shared data structure of type `linop_data_s`. (c.f. Figure 2B). Thus, data which is needed to apply the forward or the adjoint of a `linop`, for example a matrix, needs to be stored only once.

An `nlop` consists of an `operator` modeling the non-linear forward operator and `linops` which model the derivatives. For atomic `nlops`, both, the derivatives and the forward operator, have access to a shared data structure of type `nlop_data_s` (c.f. Figure 2C). This data

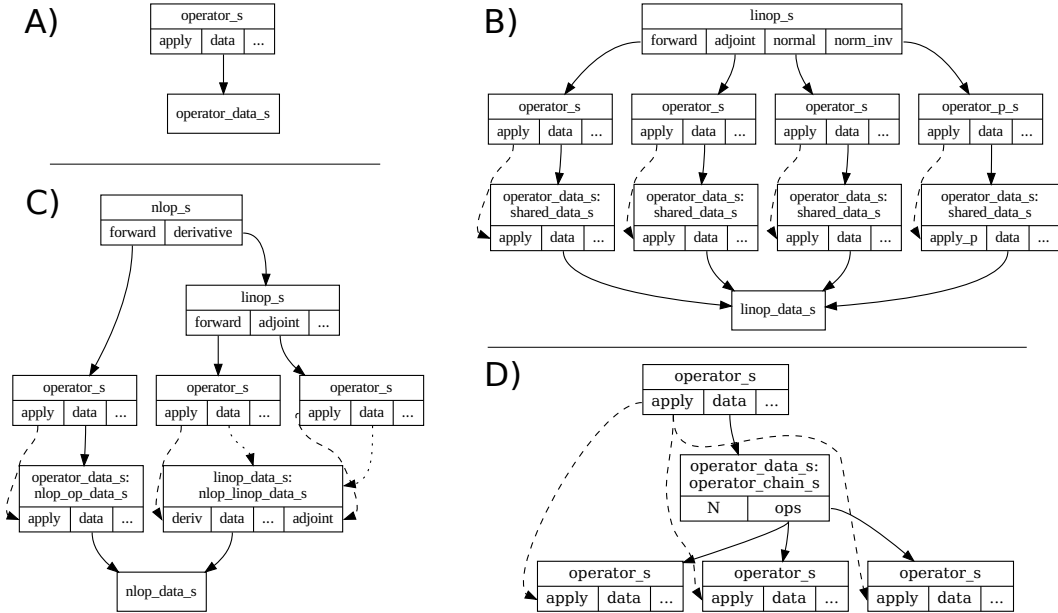


**Figure 2:** Schematic description of atomic operators, linear operators and non-linear operators as data structures in BART. Solid lines mean “points to”, dashed lines “calls (indirectly)” and dotted lines “points to indirectly”. A) An `operator` holds a reference to a data structure and a function which is called when the `operator` is applied. B) A `linop` holds references to multiple `operator`s such as the forward and adjoint operator which share a common data structure. C) An `nlop` holds references to the non-linear forward `operator` and `linop`s modeling the derivatives. The forward `operator` and `linop`s have access to a shared data structure `nlop_data.s`. D) The data structure of a chain `operator` holds references to the chained `operator`s which are applied in correct order, when the chained op is applied.

structure is used to communicate between the forward operator and the derivatives, i.e. when the forward operator is applied, it saves all information needed to apply the derivatives (for example its inputs) in the shared data structure. A simple example is the multiplication operator  $F(x, y) = xy$  with the derivative  $D_x F|_{x,y} : dx \mapsto ydx$ . When the operator is applied, the inputs  $x$  and  $y$  are stored, such that they are accessible by the derivatives. On a higher level, the structure of an atomic `nlop` is presented in Figure 3A. All shared data structures use reference counting for automatic memory management (garbage collection).

**Composing Operators** Atomic operators can be composed to more complex ones by applying them one after another. For example, two operators  $F$  and  $G$  can be chained by applying  $F$  first on some input  $x$  and apply  $G$  afterwards on the intermediate result  $F(x)$  to compute  $G(F(x))$ . The derivative of the chain  $D(G \circ F)|_x = DG|_{F(x)} \circ DF|_x$  and its adjoint  $D(G \circ F)|_x^H = DF|_x^H \circ DG|_{F(x)}^H$  can be computed by calling the (adjoint) derivatives of  $F$  and  $G$ . Consequently, we implemented the chain of two `nlops`  $F$  and  $G$  by constructing a new `nlop` holding references to  $F$  and  $G$ . When the new `nlop` is applied, it applies  $F$  and  $G$ . The derivative of the chained `nlop` is constructed by chaining the `linop`s representing the derivatives of  $F$  and  $G$  (c.f. Figure 3B). Similar to the *chain*, we provide a set of functions

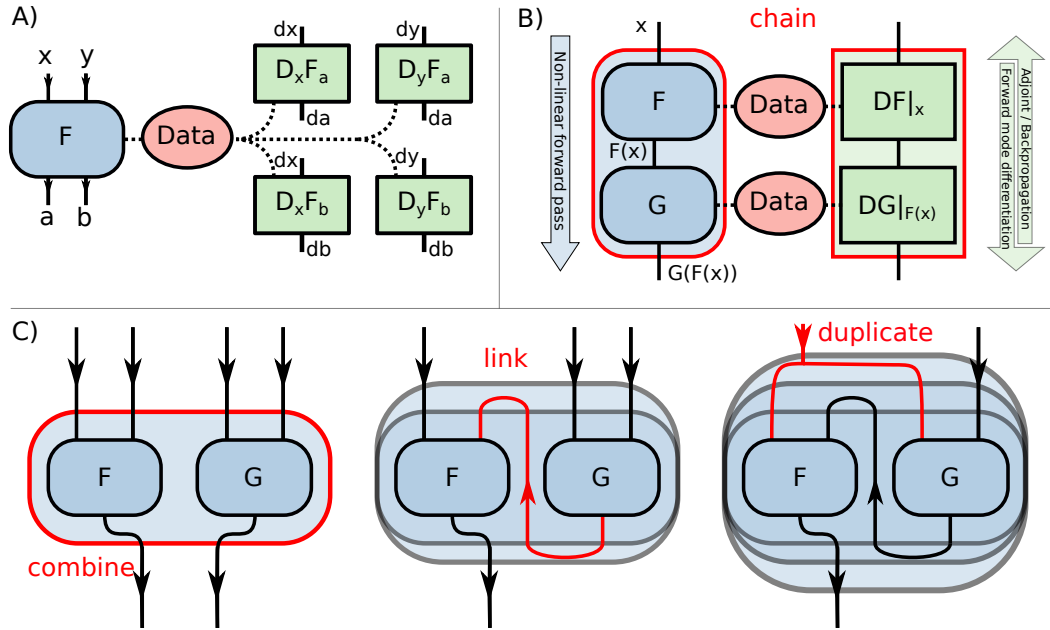


**Figure 3:** Basic concepts of nlops. A) An atomic nlop consisting of the forward operator  $F$  and its derivatives  $D_i F_o$  modeled by linops. When  $F$  is applied, it stores information in a shared data structure such that the derivatives are evaluated at the last inputs of  $F$ . B) Chaining of two nlops  $F$  and  $G$ . When the chained forward operator is applied,  $F$  is evaluated first to compute the intermediate result  $F(x)$ . Afterwards,  $G$  is applied to compute the final result. Both forward operators store information in their respective data structures, such that  $DF$  is evaluated at  $x$  and  $DG$  is evaluated at  $F(x)$ . C) The two nlops  $F$  and  $G$  are combined, and their inputs are linked and duplicated to form the residual structure  $F(x_1, G(x_1, x_2))$ . The derivatives of the final operator are constructed automatically (not shown).



for composing `nlops` with multiple number of inputs and outputs. The resulting `nlops` again hold references to the former ones and the derivatives are constructed automatically. These functions can be used to *combine* two `nlops` to one, to *link* an output of an `nlop` into one of its inputs, and to *duplicate* one of its inputs into another one. The action of these functions is presented in Figure 3C, where we demonstrate how two `nlops`  $F$  and  $G$  can be used to construct an `nlop` computing  $F(x_1, G(x_1, x_2))$ . In case  $F$  is a sum and  $G$  is a network, this structure corresponds to a residual network computing  $x_1 + G(x_1, x_2)$ .

**Functional Container** Generally, the execution properties of an `nlop` can be modified by encapsulating it in a container which itself is an `nlop`. We use such a container to implement checkpointing to reduce memory use. When the checkpointing-container is applied, the inputs are stored and the inner `nlop` is applied without saving data for computing its derivatives. When the derivatives are needed, the inner `nlop` is applied again using the inputs stored in the container and the data needed for the derivatives is re-computed. Thus, checkpointing can reduce the memory consumption at the price of multiple applications of the `nlop`.

Moreover, a functional container can be used to assign an `nlop` to a specific GPU. When such an `nlop` or its derivative is called, the CUDA context is switched to the selected device and all input data of the `nlop` are copied to the device. Afterwards the inner `nlop` is called which uses the selected device for all its computation and memory allocations. By calling `nlops` assigned to different GPUs from different threads in parallel, we can efficiently distribute the memory and computation of the `nlops` to multiple GPUs.

### 2.1.3 Iterative Training Algorithms

Training a neural network corresponds to minimizing the loss  $\sum_i L(\mathbf{y}_i, F(\mathbf{x}_i; \theta))$  with respect to the weights  $\theta$  (c.f. Eq. 1). Having constructed an `nlop` representing  $F$ , we chain its output into another `nlop`  $L$  to generate a loss-`nlop`. This loss-`nlop` has two types of inputs, those corresponding to weights  $\theta$  and those corresponding to data  $\mathbf{x}, \mathbf{y}$ .

For training neural networks, we have implemented incremental gradient methods such as stochastic gradient descent, Adam [25], and iPALM [26]. These algorithms are accessed using a unified interface provided, amongst other things, the loss-`nlop`, flags describing the type of the respective inputs (i.e. if an input corresponds to data or weights), the training data and the pre-initialized memory for the weights. The training dataset  $\mathbf{x}_i, \mathbf{y}_i$  is split into mini-batches and in each iteration the weights  $\theta$  are updated based on the gradient with respect to these weights.

### 2.1.4 Neural Network Library

For convenient construction of neural networks based on `nlops`, we implemented the neural network (nn)-library. The nn-library allows to index the arguments (inputs and outputs) of `nlops` by meaningful names instead of numeric indices. The arguments are annotated by a type defining how the optimization algorithm treats this argument (weights, data, moving statistics of batch normalization) and inputs corresponding to weights can be attached with an initializer. Moreover, the nn-library contains our implementations of typical operators used to construct neural networks, i.e.

- fully-connected (dense) layers

- convolutional layers
- batch normalization layer [27]
- activation layers: ReLU, sigmoid and softmax
- loss functions: mean squared error (MSE), mean absolute difference, structural similarity index measure (SSIM)[28], generalized dice loss [29] and categorical cross-entropy.

We stress again that our implementation works with complex valued data, i.e. real multiplications are replaced by complex ones in the fully-connected and convolutional layers. Complex convolutions with  $F$  channels can be interpreted as real convolutions with  $2F$  channels but imposing an additional symmetry on the weights [30, 31]. Complex sigmoid and ReLU activations compute the corresponding real activations independently on the real and imaginary part, i.e. ReLU is implemented as  $\mathbb{C}\text{ReLU}(x) = \text{ReLU}(\text{Re}[x]) + i\text{ReLU}(\text{Im}[x])$ .

**Integration of TensorFlow Graphs** The `nlop` framework also serves as a generic wrapper for computation graphs exported from other deep learning frameworks. As a proof of concept, we have implemented a wrapper for TensorFlow graphs based on the TensorFlow C API<sup>1</sup>. A pre-trained neural network based on TensorFlow can be exported to a graph file which is imported by BART to construct an `nlop`. When this `nlop` is applied, the forward-pass of the TensorFlow graph is executed, while TensorFlow’s gradients are used to compute the adjoint derivative of the `nlop`. The forward derivative for the TensorFlow wrapper is not implemented.

## 2.2 Applications and Implemented Networks

To demonstrate practicability of our framework, we have implemented and trained VarNet [1] and MoDL [2]. Both networks are motivated by unrolling an optimization algorithm solving the inverse problem

$$\mathbf{x}^* = \arg \min_{\mathbf{x}} \|\mathbf{A}\mathbf{x} - \mathbf{y}\|^2 + R(\mathbf{x}). \quad (5)$$

Here,  $\mathbf{A} = \mathcal{PFC}$  is the linear SENSE operator composed of the multiplication with the Coil sensitivity maps, the Fourier transform, and the projection to the sampling Pattern.  $\mathbf{x}$  is the MR image to be reconstructed and  $\mathbf{y}$  is the measured k-space data.  $R(\mathbf{x})$  is a regularization term imposing prior knowledge on the reconstructed image  $\mathbf{x}$ .

In this subsection, we first describe the structure of both networks and our respective implementations. In the second part, we describe how the TensorFlow wrapper can be used to integrate an externally trained regularizer  $R(\mathbf{x})$  for reconstruction with BART. Scripts to reproduce training and application of the networks will be available at <https://github.com/mrirecon/deep-deep-learning-with-bart>.

### 2.2.1 Variational Network

VarNet is motivated by solving Eq. 5 using an unrolled gradient descent algorithm that includes a trained regularizer  $R$ . The network is initialized with the adjoint reconstruction

<sup>1</sup>[https://www.tensorflow.org/install/lang\\_c](https://www.tensorflow.org/install/lang_c)

$\mathbf{x}^0 = A^H \mathbf{y}$  and updates the reconstruction  $\mathbf{x}^t$  by

$$\mathbf{x}^{t+1} = \mathbf{x}^t - \sum_{i=1}^{N_k} (K_i^t)^T \Phi_i^{\prime} (K_i^t \mathbf{x}^t) - \lambda^t (A^H A \mathbf{x}^t - A^H \mathbf{y}), \quad 0 \leq t \leq T - 1. \quad (6)$$

Here, the sum corresponds to the gradient of a regularizer  $R^t(\mathbf{x}) = \sum_{i=1}^{N_k} \Phi_i^t(K_i^t \mathbf{x})$ , where  $K$  is a convolution with  $N_k$  filters and  $\Phi'$  is the derivative of a trainable activation function. The imaginary part of the convolved images  $K_i^t \mathbf{x}$  is discarded to be consistent with the original implementation of VarNet. The last term corresponds to a gradient step of the data-consistency term  $\|A\mathbf{x} - \mathbf{y}\|_2^2$  with trained step size  $\lambda^t$ . For further details, we refer to [1].

The BART implementation of VarNet can be trained and applied with the `reconet` command of the BART toolbox, i.e.

```
$ bart reconet --network=varnet --train <kspace> <coils> <weights> <reference>
$ bart reconet --network=varnet --apply <kspace> <coils> <weights> <output>
```

Further options, such as network parameters, training losses and the training algorithm can be configured using command line options. The default parameter, the training algorithm and the initialization of the weights are based on the original TensorFlow implementation<sup>2</sup>, i.e. the parameter are set to  $T = 10$  iterations,  $N_k = 48$  convolution filter and  $N_w = 31$  Gaussian radial basis functions to construct the activation  $\Phi'$ . iPALM is used as training algorithm. The `--normalize` option is used to scale the data such that  $1 = \max |\mathbf{x}^0|$  holds. As our implementation is equivalent to the original one, weights trained with TensorFlow can be exported for inference with BART.

### 2.2.2 MoDL

The MoDL [2] network is another unrolled network initialized with  $\mathbf{x}^0 = A^H \mathbf{y}$ . A residual network  $\mathcal{D}_W$  denoises the current reconstruction and data-consistency is imposed by a proximal mapping. The iterations read

$$\begin{aligned} \mathbf{x}^{t+1} &= \arg \min_{\mathbf{x}} \left[ \|A\mathbf{x} - \mathbf{y}\|^2 + \lambda \|\mathbf{x} - \mathcal{D}_W(\mathbf{x}^t)\|^2 \right] \\ &= \underbrace{(A^H A + \lambda \mathcal{I})^{-1}}_{\mathcal{Q}} (A^H \mathbf{y} + \lambda \mathcal{D}_W(\mathbf{x}^t)) \end{aligned} \quad 0 \leq t \leq T - 1. \quad (7)$$

The residual network  $\mathcal{D}_W$  consists of  $L$  convolutional layers with  $F_r$  filters followed by batch normalization layers and—excepting the last layer—ReLU activation functions.

MoDL can be trained using the same `reconet` command as used for VarNet by selecting the `--network=modl` option. By default, MoDL is trained using Adam and the network parameter are based on the original TensorFlow implementation<sup>3</sup>, i.e.  $L = 5$  layers are used, and their weights are shared across the  $T = 10$  unrolled iterations. Since our implementation is based on complex-valued convolutions, we use  $F_c = 32$  complex-valued filters instead of  $F_r = 64$  real-valued filters.

<sup>2</sup><https://github.com/VLOGroup/mri-variationalnetwork>, Commit: 4b6855f

<sup>3</sup><https://github.com/hkaggarwal/modl>, Commit: 428ef84

To compute  $\mathcal{Q}(\mathbf{x})$ , we have implemented a generic inversion module which can invert any positive-definite self-adjoint linear operator  $S_\lambda : \mathbb{C}^N \rightarrow \mathbb{C}^N$  parametrized with parameters  $\lambda \in \mathbb{C}^M$ . In case of MoDL,  $S_\lambda = A^H A + \lambda \mathcal{I}$  and  $\lambda$  is just one real-valued parameter, however, the same implementation could be for example used to interpret the coil sensitivity maps as parameters of  $A$  as needed for networks jointly estimating coil sensitivity maps and image content [32]. Given an `nlop`  $\mathcal{S}$  which applies the parametrized linear operator  $S_\lambda$ , we construct the `nlop`  $\mathcal{S}^{-1}$  applying the inverse  $S_\lambda^{-1}$ . These `nlops` are defined by

$$\begin{aligned} \mathcal{S} : \mathbb{C}^N \times \mathbb{C}^M &\rightarrow \mathbb{C}^N & \mathcal{S}^{-1} : \mathbb{C}^N \times \mathbb{C}^M &\rightarrow \mathbb{C}^N \\ (\mathbf{x}, \lambda) &\mapsto \mathbf{y} = S_\lambda \mathbf{x} & (\mathbf{y}, \lambda) &\mapsto \mathbf{x} = S_\lambda^{-1} \mathbf{y} . \end{aligned}$$

The derivatives of  $\mathcal{S}^{-1}$  are given by

$$\begin{aligned} D_{\mathbf{x}} \mathcal{S}^{-1} |_{\mathbf{x}, \lambda} : d\mathbf{x} &\mapsto d\mathbf{y} = S_\lambda^{-1} d\mathbf{x} \\ D_{\lambda} \mathcal{S}^{-1} |_{\mathbf{x}, \lambda} : d\lambda &\mapsto d\mathbf{y} = -S_\lambda^{-1} \circ D_{\lambda} \mathcal{S} |_{\mathbf{y}=\mathcal{S}^{-1}(\mathbf{x}, \lambda), \lambda} d\lambda . \end{aligned}$$

As proposed in [2], we use the conjugate gradient algorithm to apply  $S_\lambda^{-1}$ . The derivative with respect to the parameters  $\lambda$  involves the derivative of  $\mathcal{S}$  evaluated at the result of the forward path  $\mathbf{y} = \mathcal{S}^{-1}(\mathbf{x}, \lambda)$ . This derivative is computed using the `nlop`  $\mathcal{S}$ .

### 2.2.3 Extensions to the SENSE-Model

BART’s implementation of the SENSE model is generic in the sense that it can handle multiple sets of coil sensitivity maps (soft-SENSE, c.f. [33]) and supports non-Cartesian sampling patterns. The soft-SENSE model is suitable if the object exceeds the FOV since one set of coil sensitivity maps can not explain infolding artifacts [33]. In the context of deep-learning, the soft-SENSE model has been used recently in [34, 35]. BART’s implementations of VarNet and MoDL only uses the image corresponding to the first set of coil sensitivity maps in the network part of the soft-SENSE model. For training the soft-SENSE networks, we use the MSE as loss and the coil images as ground-truth since the coil images serve as a reference independent of the estimated coil sensitivity maps.

Reconstruction networks for non-Cartesian sampling trajectories have been investigated recently in [36, 37, 38], where [37, 38] make use of the PyTorch implementation of the non-uniform FFT [39]. Our implementations of VarNet and MoDL utilize the non-uniform (nu) FFT in BART which implemented as a linear operator. The nuFFT in Eqs. 6 and 7 is needed once to compute the adjoint  $A^H \mathbf{y}$  and afterwards only in the combined forward and adjoint operator  $\mathcal{F}^H \mathcal{P}^H \mathcal{P} \mathcal{F}$ . To save expensive gridding steps of the nuFFT, we precompute the adjoint reconstruction for the whole dataset. The forward-backward nuFFT  $\mathcal{F}^H \mathcal{P}^H \mathcal{P} \mathcal{F}$  is computed efficiently using the precomputed point-spread function and the Toeplitz trick [40, 41], which significantly speeds up computations on the GPU [42, 43].

For non-Cartesian trajectories, we initialize the network with a Tikhonov-regularized SENSE reconstruction  $\mathbf{x}_0 = \mathcal{Q} A^H \mathbf{y}$  with  $\lambda = 0.1$  normalized to a maximum magnitude of one instead of the adjoint reconstructions. The resulting initial reconstruction is normalized to have a maximum magnitude of one. For MoDL, the number of CG-iterations in each data-consistency block has been increased from 10 to 30, while the number of unrolled iterations has been reduced to  $T = 5$ .

### 2.3 Image Reconstruction using a Learned Prior

An alternative approach of using neural networks for MRI reconstruction is learning prior knowledge about the image distribution by learning a regularizer  $R(\mathbf{x})$  independently of the reconstruction. For reconstruction, the learned regularizer is inserted into Eq. 5. One approach to learn a regularizer is based on deep Bayesian estimation [16]. The resulting regularizer is given by

$$R(\mathbf{x}) = -\lambda \log p(\mathbf{x}; \text{Net}(\mathbf{x}, \Theta^*)). \quad (8)$$

Here,  $\text{Net}(\mathbf{x}, \Theta^*)$  denotes the PixelCNN++ [44] which is trained to predict the conditioned distribution parameters of the mixture of logistic distributions that are used to model the image distribution. Inserting the regularizer  $R$  defined in Eq. 8 into the optimization problem Eq. 5 corresponds to a maximum a posteriori estimation for the reconstructed image. For more details, we refer to the original publication [16].

For reconstruction, the trained TensorFlow graph representing  $-\log p(\mathbf{x}; \text{Net}(\Theta^*, \mathbf{x}))$  is exported and loaded into BART using the TensorFlow wrapper described above. The resulting `nlop` is used to construct the corresponding proximal operator

$$\text{prox}_R(\mathbf{v}) = \arg \min_{\mathbf{x}} \frac{1}{2} \|\mathbf{x} - \mathbf{v}\|^2 + R(\mathbf{x}). \quad (9)$$

The solution of the proximal operator is obtained by the gradient descent algorithm, where the gradients of the regularizer  $R$  can be computed using automatic differentiation. The proximal operator can be plugged into any of BART’s proximal operator based iterative optimization algorithms. Reconstruction based on any TensorFlow graph representing a regularizer can be performed using the `pics` command, i.e.

```
$ bart pics -R TF:{model_path}:lambda <kspace> <sensitivities> <output>
```

## 3 Results

### 3.1 Reconstructions with BART

To compare the reconstruction quality of our implementations of VarNet and MoDL with the TensorFlow implementations, we have trained both networks using the datasets provided with the respective publications. In the following, the dataset published with the VarNet is referred to as `knee-dataset` and the dataset published with MoDL is referred to as `brain-dataset`. VarNet was trained for 30 epochs algorithm with a batch size  $N_b = 10$  on 300 slices of 15 subjects from the `coronal_pd.fs` directory, while the 20 central slices of the remaining 5 subjects were used for evaluation. MoDL was trained with batch size  $N_b = 10$  in a two-step-approach, i.e. the weights were initialized for 100 epochs using  $T = 1$  unrolled iteration and afterwards the network was trained for 50 epochs with  $T = 10$ . For evaluation, the central 100 slices from the test dataset were used. The default network parameters described in the methods part were used for both networks and only the input data of VarNet were normalized. We show example reconstructions based on the respective networks and implementations in Figure 4. Both implementations of the respective networks perform quite similar and better than the classical  $\ell_1$ -Wavelet regularized compressed sensing reconstruction. The TensorFlow

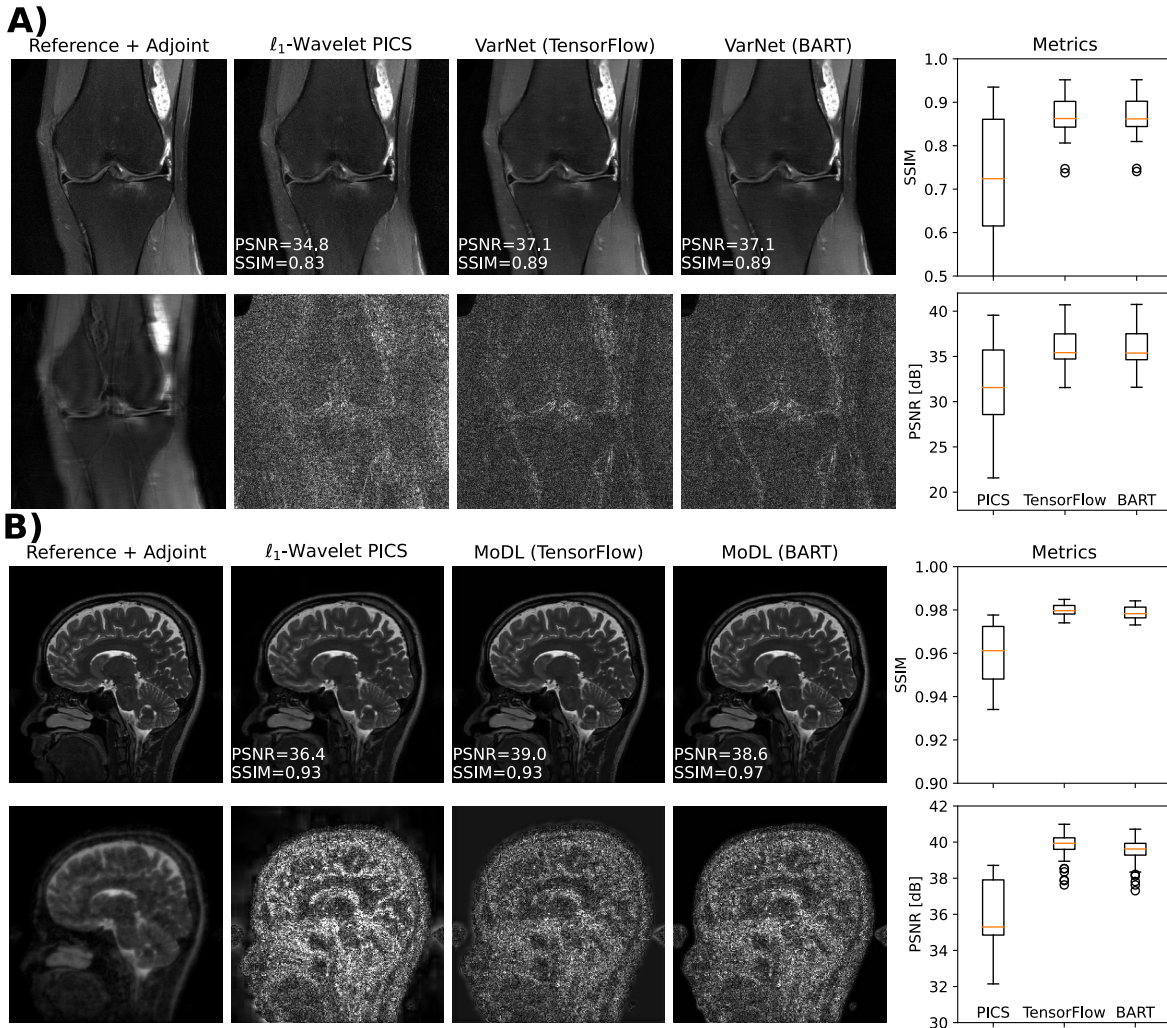


**Figure 4:** Comparison of the TensorFlow and BART implementation of VarNet (A) and MoDL (B). For reference, we also show the results of an  $\ell_1$ -Wavelet regularized SENSE reconstruction computed using the BART pics tool. The fully-sampled k-space of the reference knee image in (A) was retrospectively subsampled using a regular sampling pattern with a spacing of four along the phase encoding dimension and 28 auto-calibration lines. The resulting k-space data was reconstructed with the respective methods. The reference brain image in (B) was multiplied with the coil sensitivity maps, Fourier transformed, subsampled using a 2D variable density mask with acceleration factor 6, disturbed with additive white Gaussian noise, and, finally, reconstructed with the respective reconstruction methods. The boxplots are based on the PSNR and SSIM computed for 100 images of the respective evaluation datasets. For this comparison, we used the coil sensitivities as foreground mask which explains the discrepancy to the SSIM values given at the reconstructed images.

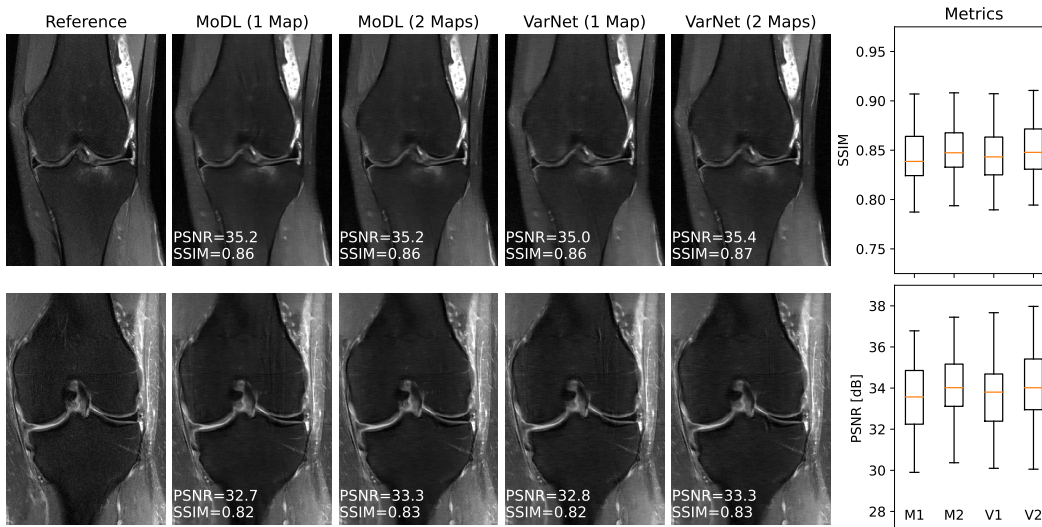


**Figure 5:** Comparison of two example reconstructions with MoDL and VarNet using one set of coil sensitivity maps (regular SENSE) and two sets of coil sensitivity maps (soft-SENSE). The aliased k-space data is simulated by first zero-padding the fully-sampled coil-images and afterwards sub-sampling the k-space by a factor of two before applying the usual sampling pattern (every fourth line and 28 auto calibration lines). Especially the bottom example suffers under-sampling artifacts if only one set of coil sensitivity maps is used.

implementation has a lower SSIM in the example reconstruction due to an offset in the background. To have a fair comparison based on the image content, we used the coil sensitivity maps as a foreground mask to compute the PSNR and SSIM of the respective evaluation datasets. We present the resulting metrics as box plots in Figure 4. Both implementations of the respective networks perform similar in terms of PSNR and SSIM.

To demonstrate the benefits of the soft-SENSE model in the case that the object exceeds the FOV, we simulated k-space data with a reduced FOV from the fully-sampled knee dataset and trained VarNet and MoDL on this dataset with the respective default parameters described above. ESPIRiT [33] was used to estimate either one or two sets of coil sensitivity maps from the simulated k-space. Two example reconstructions based on MoDL and VarNet using one or two sets of coil sensitivity maps are shown in Figure 5. We also compute the PSNR and SSIM of the evaluation dataset and present the results in the boxplots in Figure 5. Reconstructions using two sets of coil sensitivity maps show less aliasing artifacts and are superior in terms of SSIM and PSNR.

We have also used the knee-dataset to simulate non-Cartesian k-space data by applying the nuFFT on each coil image independently. In Figure 6, we present an example reconstruction using the non-Cartesian versions of VarNet and MoDL. The learned methods improve the image quality compared to the classical  $\ell_1$ -Wavelet regularized reconstruction slightly.

### 3.2 Computational Performance

Training a neural network is a computationally demanding task, making the training time a possible bottleneck for the application of neural networks in MRI reconstructions. To compare



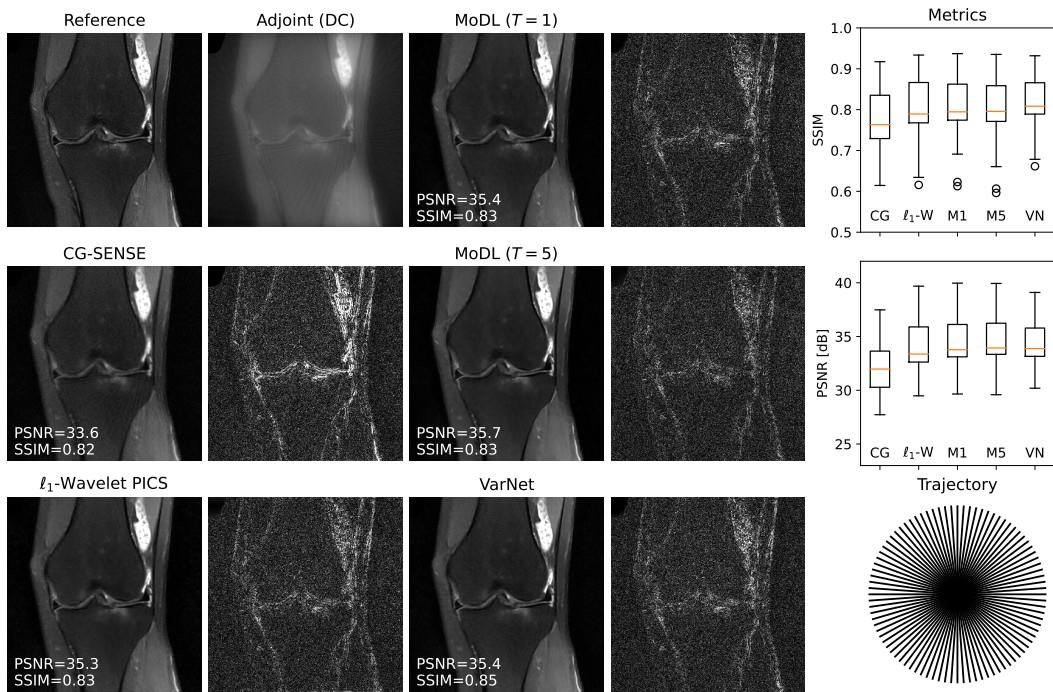


**Figure 6:** Comparison of MoDL and VarNet for non-Cartesian reconstructions using a radial trajectory with 44 spokes. The fully-sampled k-space data from the reference knee image in Figure 4 was interpolated on the trajectory to simulate the non-Cartesian k-space data. Both networks are initialized with a CG-SENSE reconstruction. For reference, we show the results of a CG-SENSE and  $\ell_1$ -Wavelet regularized reconstruction computed using the BART pics tool. The difference images are scaled by a factor 10.



the computational performance of our implementation with those based on TensorFlow<sup>4</sup>, we measured the training and inference time of MoDL and VarNet on four different NVIDIA GPUs for all implementations. We use a version of TensorFlow 1.15 maintained by NVIDIA to support newer GPUs<sup>5</sup> with cuBLAS 11.7, and cuFFT 10.6, cuDNN 8.3. For VarNet we also measured the training time using the prior implementation<sup>6</sup> based on TensorFlow-ICG<sup>7</sup>. The training time of BART was measured using one and two GPUs once with CUDA 11.2, cuDNN 8.3 and the use of non-deterministic algorithm and once without cuDNN and only using deterministic algorithms. All model parameters were chosen as described above except the number of unrolled iterations of MoDL which had to be reduced to  $T = 5$  to fit in the 12 GB GPU memory with a batch size of  $N_b = 10$ . For MoDL, only the time for the second part of the two-step training has been measured. The results are presented in Figure 7. The network block of MoDL is not distributed to multiple GPUs since the batch-normalization makes slices in one batch depend on each other. On the older GPUs MoDL still benefits from the parallelization of the data-consistency block. VarNet is fully parallelized over the two GPUs such that training time is almost halved by doubling the number of GPUs. The inference time was measured on the respective evaluation datasets. To reduce the bias due to different pre-processing procedures on the CPU in the respective implementations, we also measured the total execution time of GPU kernels using NVIDIA Nsight Systems. In general, the BART implementations achieve similar performance to the TensorFlow implementations.

Another critical limit is the memory consumption of the networks on the GPU. We measured the peak GPU memory allocation during training and inference for the respective implementations of MoDL and VarNet and present the results in Table 1. Since allocating GPU memory is expensive, both, BART and TensorFlow, use a memory cache to reuse allocated memory. While BART allocates memory on demand, TensorFlow pre-allocates larger memory blocks which might not be necessary. Thus, we also provide the memory usage before reaching the peak usage which serves as a loose lower bound for the memory needed by TensorFlow. BART needs more memory than TensorFlow to train MoDL but less memory to train VarNet. The memory needed for inference is similar across implementations.

### 3.3 Image Reconstruction using a Learned Prior

In Figure 8, we present the reconstruction based on a learned prior. Data was acquired on a Siemens Skyra 3T scanner (Siemens Healthcare GmbH, Erlangen, Germany). For reconstruction, we used 60 spokes of a radial Flash sequence ( $TR=770\text{ms}$ ,  $TE=16\text{ms}$ ,  $FA=18^\circ$ ). The coil sensitivity maps were estimated using ESPIRiT and gradient delays were corrected based on RING [45]. We compare a reconstruction using the inverse nuFFT, an  $\ell_1$ -Wavelet regularized PICS reconstruction and a reconstruction using the learned log-likelihood prior (c.f. Eq. 8). The learned log-likelihood prior results in an improved reconstruction compared to the classical  $\ell_1$ -Wavelet regularized reconstruction.

<sup>4</sup>VarNet: <https://github.com/VLOGroup/mri-variationalnetwork>, Commit: 653630b; MoDL: <https://github.com/hkaggarwal/modl>, Commit: 428ef84

<sup>5</sup><https://github.com/NVIDIA/tensorflow>

<sup>6</sup><https://github.com/VLOGroup/mri-variationalnetwork>, Commit: 4b6855f

<sup>7</sup><https://github.com/VLOGroup/tensorflow-icg>; CUDA 8.0; cuDNN 7.0

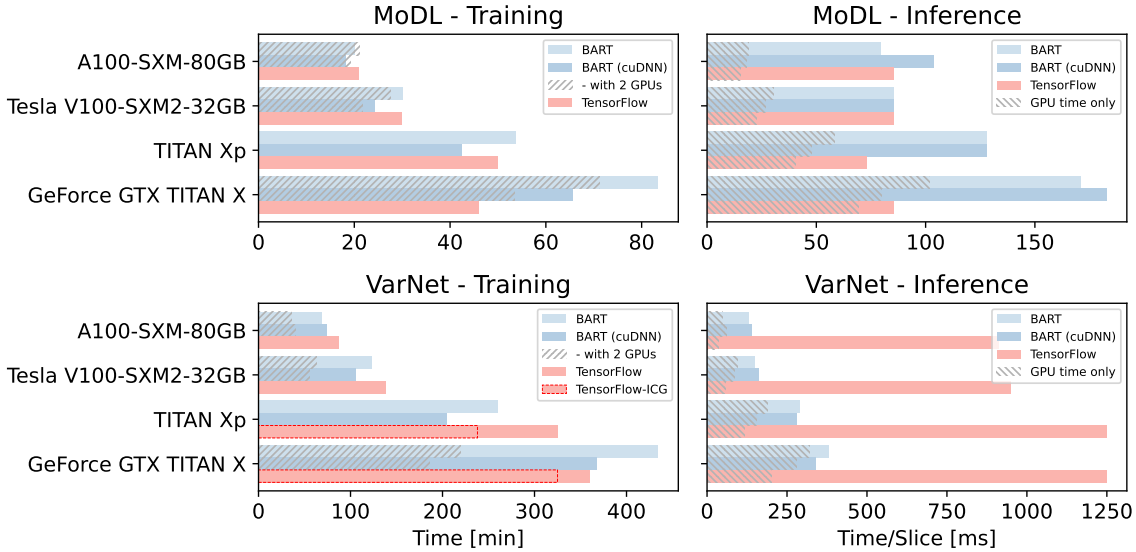


**Figure 7:** Comparison of training (left) and inference (right) time for MoDL and VarNet on different GPUs. The use of two GPUs almost halves training time for VarNet while MoDL does not benefit as much from multiple GPUs since batch-normalization in the denoising blocks requires synchronization. We observed slow host to device copies on the TITAN Xp which might explain the comparably low performance of the TensorFlow implementation of MoDL on this GPU. In general, the BART and TensorFlow implementations provide similar performance.

	Training			Inference		
	BART	+ cuDNN	TensorFlow	BART	+ cuDNN	TensorFlow
MoDL						
A100	11770	12388	9686 (5534)	2152	2478	1838 (1312)
V100	11514	11770	9158 (2746)	1896	2012	1372 (1058)
TITAN Xp	11251	12063	8811 (4701)	1663	1687	3841 (685)
GTX TITAN X	11116	11980	8753 (4636)	1508	1566	3793 (599)
VarNet						
A100	6504	6882	17874 (9682)	1642	2094	1840 (1584)
V100	6248	6392	17354 (9162)	1384	1628	1376 (1002)
TITAN Xp	6003	6053	11825 (8817)	1139	1309	1027 (771)
GTX TITAN X	5938	6000	11835 (8765)	1066	1144	981 (480)

**Table 1:** GPU-Memory usage in MiB of MoDL and VarNet using the respective implementations of the networks on different GPUs (A100-SXM-80GB, Tesla V100-SXM2-32GB, TITAN Xp and GeForce GTX TITAN X). As TensorFlow allocates more memory than necessary, we provide the memory usage before reaching the peak usage in parentheses. This value serves as a loose lower bound. For training MoDL, BART needs more memory than TensorFlow while BART needs less memory to train VarNet. The memory needed for inference is similar across implementations.

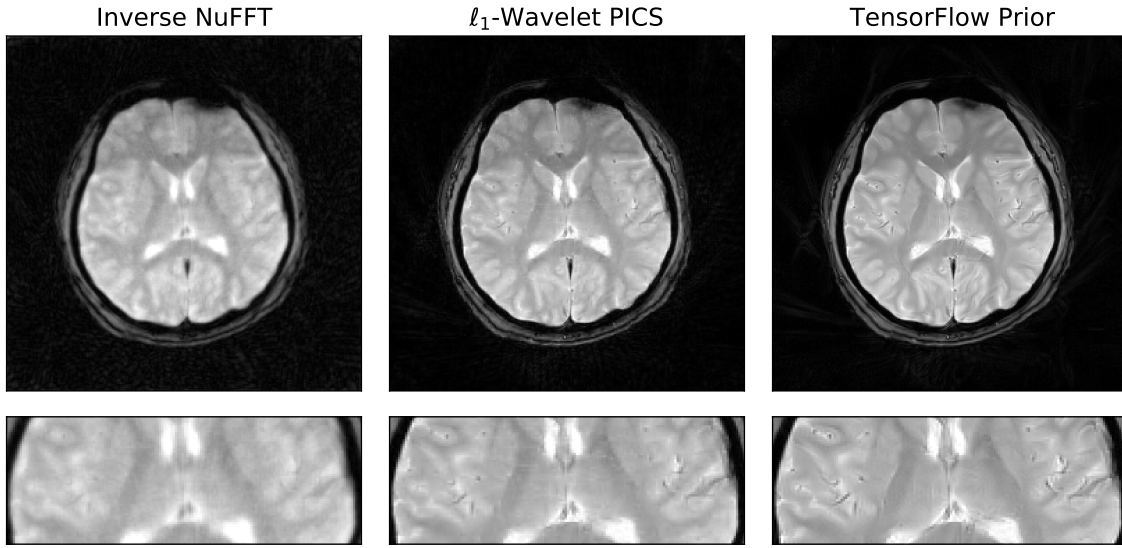


**Figure 8:** Brain images reconstructed from 60 radial k-space spokes via a coil-combined inverse nuFFT, an  $\ell_1$ -Wavelet regularized PICS reconstructions, and a PICS reconstruction using a learned log-likelihood prior (left to right).

## 4 Discussion

In this work, we describe a framework for deep learning that was included in the BART toolbox. The framework is based on an extension of the existing non-linear operator framework in BART that provides automatic differentiation and directly integrates BART’s existing MRI-specific operators such as multidimensional FFT, nuFFT, and SENSE operators and complements it with many operators commonly used to construct neural networks. A sophisticated framework for constructing complex neural networks was added. We also implemented various optimizing techniques and achieve computational performance similar to other deep-learning frameworks. Distributing computation to multiple GPUs can reduce computation time further. Finally, we added new optimization algorithms such as stochastic gradient descent, iPALM, and Adam, which are popular for training neural networks. To demonstrate practicality of the framework, we implemented and trained the Variational Network and MoDL in BART. Our implementation achieves similar performance in terms of reconstruction quality and training time compared to the original implementations based on TensorFlow. Further, BART’s generic formulation of the SENSE model including the non-Cartesian and soft-SENSE formulation together with a flexible parametrization of the training procedure in terms of training algorithm, loss functions, and training target (coil combined reconstruction, RSS reconstruction or coil images) enables direct use of VarNet and MoDL for many applications.

State-of-the-art deep-learning-based MR image reconstruction algorithms combine two fields of research, i.e. the field of machine learning and the field of classical MRI reconstruction methods. For both fields, mature software frameworks/toolboxes already exist. Hence, various approaches exist to develop algorithms combining both fields, the two extreme cases

are 1.) MRI specific operations can be re-implemented in deep-learning frameworks and 2.) neural networks can be re-implemented in MRI frameworks. Both approaches have different advantages and disadvantages. Deep learning frameworks such as TensorFlow or PyTorch are driven by large communities and recent developments in the field of deep learning are quickly integrated. Moreover, many tutorials based on standard frameworks exist and simple scripting based on Python reduces the barrier to entry. The frameworks are designed for large scale datasets and support most recent hardware as well as direct integration into cloud solutions of various providers. However, all these features come at a price: Current deep learning libraries use many external libraries with complex dependencies. Updating some libraries in the backend or the framework itself might produce version conflicts which are hard to resolve. Long-term reproducibility of research results is difficult to achieve in this environment. One solution is to freeze the environment in a software container which contains the specific software versions that are known to work. In this way, containers can facilitate the reproduction of results and the translation of working setups to clinical pipelines [46, 47]. While freezing setups is a legitimate approach for production environments or reproducing results, it is not a sustainable solution for long term research and development, where new developments need to build on top of existing code.

On the other side, BART is designed for rapid prototyping, reproducible research and clinical translation. It depends only on a few external libraries such as FFTW, BLAS implementations or — if compiled with GPU support — CUDA, making it simple to integrate into different software environments. Where standard deep learning frameworks benefit from large community support integrating new deep learning features, BART benefits from years of research on MR image reconstruction. For example, a crucial part of most multi-coil reconstruction networks is the estimation of the coil sensitivity maps in a preprocessing step. Since BART implements several calibration methods such as ESPIRiT or NLINV, a full reconstruction pipeline based on Variational Network or MoDL can be implemented completely in BART. Advanced concepts from MRI implemented in BART can be directly used in these machine learning methods. For example, our data consistency modules are implemented using a generalized SENSE model supporting multiple sets of coil sensitivity maps and non-Cartesian trajectories. Concerning performance of training neural networks, we have demonstrated that BART can compete with the TensorFlow implementation of MoDL and VarNet. BART development makes use of a continuous integration framework that uses automatic testing. Based on this, we aim for long-term reproducibility of published results even with new BART versions. Finally, BART is already widely used in the community of MRI research and also used for clinical research as part of automatic reconstruction frameworks such as Gadgetron [46, 48] or Yarra [49]. Thus, we believe that the integration of neural networks into BART will also facilitate research and clinical translation of deep learning methods for image reconstruction.

## 5 Conclusion

By integrating a complete set of tools for training and using neural networks into BART, we provide a general framework for research in image reconstruction that combines state-of-the-art methods for image reconstruction with deep-learning-based methods. The implementation of two recent deep-learning-based methods in BART demonstrates similar performance as

their original TensorFlow-based implementations.

## Conflict of Interest

The authors declare no competing interests.

## Open Research

### Data Availability Statement

In the spirit of reproducible research, code to reproduce the experiments will be available on <https://github.com/mrirecon/deep-deep-learning-with-bart>. BART itself is available on <https://github.com/mrirecon/bart>. The data that support the findings of this study are available from the publications of the Variational Network [1] and MoDL [2]. Data are available at [https://app.globus.org/file-manager?origin\\_id=15c7de28-a76b-11e9-821c-02b7a92d8e58&origin\\_path=%2F](https://app.globus.org/file-manager?origin_id=15c7de28-a76b-11e9-821c-02b7a92d8e58&origin_path=%2F) (VarNet) and <https://drive.google.com/file/d/1qp-19kJbRfQU1W5wCj0QZi7I3T6jwA37/view?usp=sharing> (MoDL).

## Acknowledgements

This work was funded by the "Niedersächsisches Vorab" funding line of the Volkswagen Foundation, and funded in part by NIH under grant U24EB029240 and funded in part by the Deutsche Forschungsgemeinschaft (DFG, German Research Foundation) under grant UE 189/1-1, under Germany's Excellence Strategy - EXC 2067/1- 390729940, and with Project-ID 432680300 - SFB 1456. This work was supported by the DZHK (German Centre for Cardiovascular Research). We gratefully acknowledge the support of the NVIDIA Corporation with the donation of one NVIDIA TITAN Xp GPU for this research.

## References

- [1] Hammernik K, Klatzer T, Kobler E, Recht MP, Sodickson DK, Pock T, Knoll F. Learning a variational network for reconstruction of accelerated MRI data. *Magn. Reson. Med.* 2017; 79:3055–3071.
- [2] Aggarwal HK, Mani MP, Jacob M. MoDL: Model-Based Deep Learning Architecture for Inverse Problems. *IEEE Transactions on Medical Imaging* 2019; 38:394–405.
- [3] Sodickson DK, Manning WJ. Simultaneous acquisition of spatial harmonics (SMASH): fast imaging with radiofrequency coil arrays. *Magn. Reson. Med.* 1997; 38:591–603.
- [4] Griswold MA, Jakob PM, Heidemann RM, Nittka M, Jellus V, Wang J, Kiefer B, Haase A. Generalized autocalibrating partially parallel acquisitions (GRAPPA). *Magn. Reson. Med.* 2002; 47:1202–1210.
- [5] Lustig M, Pauly JM. SPIRiT: Iterative self-consistent parallel imaging reconstruction from arbitrary k-space. *Magn. Reson. Med.* 2010; 64:457–471.

- [6] Pruessmann KP, Weiger M, Scheidegger MB, Boesiger P. SENSE: sensitivity encoding for fast MRI. *Magn. Reson. Med.* 1999; 42:952–962.
- [7] Lustig M, Donoho D, Pauly JM. Sparse MRI: The application of compressed sensing for rapid MR imaging. *Magn. Reson. Med.* 2007; 58:1182–1195.
- [8] Block KT, Uecker M, Frahm J. Undersampled radial MRI with multiple coils. Iterative image reconstruction using a total variation constraint. *Magn. Reson. Med.* 2007; 57:1086–1098.
- [9] Liang D, Liu B, Wang J, Ying L. Accelerating SENSE using compressed sensing. *Magn. Reson. Med.* 2009; 62:1574–1584.
- [10] Abadi M, Barham P, Chen J, Chen Z, Davis A, Dean J, Devin M, Ghemawat S, Irving G, Isard M, Kudlur M, Levenberg J, Monga R, Moore S, Murray DG, Steiner B, Tucker P, Vasudevan V, Warden P, Wicke M, Yu Y, Zheng X. TensorFlow: A system for large-scale machine learning. In: 12th USENIX Symposium on Operating Systems Design and Implementation (OSDI 16), Savannah, Georgia, USA, 2016. pp. 265–283.
- [11] Paszke A, Gross S, Massa F, Lerer A, Bradbury J, Chanan G, Killeen T, Lin Z, Gimelshein N, Antiga L, Desmaison A, Kopf A, Yang E, DeVito Z, Raison M, Tejani A, Chilamkurthy S, Steiner B, Fang L, Bai J, Chintala S. PyTorch: An Imperative Style, High-Performance Deep Learning Library. *in* “Advances in Neural Information Processing Systems 32” (Wallach H, Larochelle H, Beygelzimer A, d’AlchéBuc F, Fox E, Garnett R, Eds.), pp. 8024–8035. Curran Associates, Inc., 2019.
- [12] Sawyer AM, Lustig M, Alley M, Uecker P, Virtue P, Lai P, Vasanawala S, Healthcare G. Creation of Fully Sampled MR Data Repository for Compressed Sensing of the Knee. SMRT 22nd Annual Meeting, Salt Lake City, 2013.
- [13] Ong F, Amin S, Vasanawala S, Lustig M. mridata.org: An Open Archive for Sharing MRI Raw Data. In: *Proc. Intl. Soc. Mag. Reson. Med.*, Paris, 2018. p. 3425.
- [14] Knoll F, Murrell T, Sriram A, Yakubova N, Zbontar J, Rabbat M, Defazio A, Muckley MJ, Sodickson DK, Zitnick CL, Recht MP. Advancing machine learning for MR image reconstruction with an open competition: Overview of the 2019 fastMRI challenge. *Magn. Reson. Med.* 2020; 84:3054–3070.
- [15] Zhu B, Liu JZ, Cauley SF, Rosen BR, Rosen MS. Image reconstruction by domain-transform manifold learning. *Nature* 2018; 555:487–492.
- [16] Luo G, Zhao N, Jiang W, Hui ES, Cao P. MRI reconstruction using deep Bayesian estimation. *Magn. Reson. Med.* 2020; 84:2246–2261.
- [17] Yang G, Yu S, Dong H, Slabaugh G, Dragotti PL, Ye X, Liu F, Arridge S, Keegan J, Guo Y, Firmin D. DAGAN: Deep De-Aliasing Generative Adversarial Networks for Fast Compressed Sensing MRI Reconstruction. *IEEE Trans. Med. Imag.* 2018; 37:1310–1321.
- [18] Kofler A, Haltmeier M, Schaeffter T, Kachelrieß M, Dewey M, Wald C, Kolbitsch C. Neural networks-based regularization for large-scale medical image reconstruction. *Phys. Med. Biol.* 2020; 65:135003.

- [19] Schlemper J, Caballero J, Hajnal JV, Price AN, Rueckert D. A Deep Cascade of Convolutional Neural Networks for Dynamic MR Image Reconstruction. *IEEE Trans. Med. Imag.* 2018; 37:491–503.
- [20] Uecker M, Ong F, Tamir JI, Bahri D, Virtue P, Cheng JY, Zhang T, Lustig M. Berkeley advanced reconstruction toolbox. In: *Proc. Intl. Soc. Mag. Reson. Med.*, Toronto, 2015. p. 2486.
- [21] Holme HCM, Rosenzweig S, Ong F, Wilke RN, Lustig M, Uecker M. ENLIVE: An Efficient Nonlinear Method for Calibrationless and Robust Parallel Imaging. *Sci. Rep.* 2019; 9:3034.
- [22] Wang X, Tan Z, Scholand N, Roeloffs V, Uecker M. Physics-based Reconstruction Methods for Magnetic Resonance Imaging. *Philos. Trans. R. Soc. A.* 2021; DOI: 10.1098/rsta.2020.0196.
- [23] Blumenthal M, Uecker M. Deep Deep Learning with BART. In: *Proc. Intl. Soc. Mag. Reson. Med.*, Virtual Conference, 2021. p. 1754.
- [24] Guanxiong L, Blumenthal M, Uecker M. Using data-driven image priors for image reconstruction with BART. In: *Proc. Intl. Soc. Mag. Reson. Med.*, Virtual Conference, 2021. p. 3768.
- [25] Kingma DP, Ba J. Adam: A Method for Stochastic Optimization, 2014.
- [26] Pock T, Sabach S. Inertial Proximal Alternating Linearized Minimization (iPALM) for Nonconvex and Nonsmooth Problems. *SIAM J. Img. Sci.* 2016; 9:1756–1787.
- [27] Ioffe S, Szegedy C. Batch Normalization: Accelerating Deep Network Training by Reducing Internal Covariate Shift. In: "Proceedings of the 32nd International Conference on Machine Learning (Bach F, Blei D, Eds.), Lille, France, 2015. pp. 448–456.
- [28] Zhao H, Gallo O, Frosio I, Kautz J. Loss Functions for Image Restoration With Neural Networks. *IEEE Trans. Comput. Imag.* 2017; 3:47–57.
- [29] Sudre CH, Li W, Vercauteren T, Ourselin S, Cardoso MJ. Generalised Dice Overlap as a Deep Learning Loss Function for Highly Unbalanced Segmentations. *in* "Deep Learning in Medical Image Analysis and Multimodal Learning for Clinical Decision Support", pp. 240–248. Springer International Publishing, 2017.
- [30] Trabelsi C, Bilaniuk O, Zhang Y, Serdyuk D, Subramanian S, Santos JF, Mehri S, Rostamzadeh N, Bengio Y, Pal CJ. Deep Complex Networks. In: 6th International Conference on Learning Representations, ICLR 2018, Conference Track Proceedings, Vancouver, British Columbia, Canada, 2018.
- [31] Cole E, Cheng J, Pauly J, Vasanawala S. Analysis of deep complex-valued convolutional neural networks for MRI reconstruction and phase-focused applications. *Magn. Reson. Med.* 2021; 86:1093–1109.

- [32] Arvinte M, Vishwanath S, Tewfik AH, Tamir JI. Deep J-Sense: Accelerated MRI Reconstruction via Unrolled Alternating Optimization. In: *Medical Image Computing and Computer Assisted Intervention*, Cham, 2021. pp. 350–360.
- [33] Uecker M, Lai P, Murphy MJ, Virtue P, Elad M, Pauly JM, Vasanawala SS, Lustig M. ESPIRiT—an eigenvalue approach to autocalibrating parallel MRI: where SENSE meets GRAPPA. *Magn. Reson. Med.* 2014; 71:990–1001.
- [34] Hammernik K, Schlemper J, Qin C, Duan J, Summers RM, Rueckert D. Systematic evaluation of iterative deep neural networks for fast parallel MRI reconstruction with sensitivity-weighted coil combination. *Magn. Reson. Med.* 2021; DOI: 10.1002/mrm.28827.
- [35] Johnson PM, Tong A, Donthireddy A, Melamud K, Petrocelli R, Smereka P, Qian K, Keerthivasan MB, Chandarana H, Knoll F. Deep Learning Reconstruction Enables Highly Accelerated Biparametric MR Imaging of the Prostate. *J. Magn. Reson. Imaging* 2021; DOI: 10.1002/jmri.28024.
- [36] Schlemper J, Salehi SSM, Kundu P, Lazarus C, Dyvorne H, Rueckert D, Sofka M. Nonuniform Variational Network: Deep Learning for Accelerated Nonuniform MR Image Reconstruction. In: *Medical Image Computing and Computer Assisted Intervention – MICCAI 2019* (Shen D, Liu T, Peters TM, Staib LH, Essert C, Zhou S, Yap PT, Khan A, Eds.), Cham, 2019. pp. 57–64.
- [37] Kofler A, Haltmeier M, Schaeffter T, Kolbitsch C. An end-to-end-trainable iterative network architecture for accelerated radial multi-coil 2D cine MR image reconstruction. *Med. Phys.* 2021; 48:2412–2425.
- [38] Ramzi Z, Starck JL, Ciuciu P. Density Compensated Unrolled Networks For Non-Cartesian MRI Reconstruction. In: *2021 IEEE 18th International Symposium on Biomedical Imaging (ISBI)*, Nice, France, 2021.
- [39] Muckley MJ, Stern R, Murrell T, Knoll F. TorchKbNufft: A High-Level, Hardware-Agnostic Non-Uniform Fast Fourier Transform. In: *ISMRM Workshop on Data Sampling & Image Reconstruction*, Sedona, Arizona, USA, 2020.
- [40] Wajer FTAW, Pruessmann KP. Major speedup of reconstruction for sensitivity encoding with arbitrary trajectories. In: *Proc. Intl. Soc. Mag. Reson. Med.*, Glasgow, 2001. p. 0767.
- [41] Fessler JA, Lee S, Olafsson VT, Shi HR, Noll DC. Toeplitz-based iterative image reconstruction for MRI with correction for magnetic field inhomogeneity. *IEEE Trans. Signal Processing* 2005; 53:3393–3402.
- [42] Uecker M, Zhang S, Frahm J. Nonlinear inverse reconstruction for real-time MRI of the human heart using undersampled radial FLASH. *Magn. Reson. Med.* 2010; 63:1456–1462.
- [43] Baron CA, Dwork N, Pauly JM, Nishimura DG. Rapid compressed sensing reconstruction of 3D non-Cartesian MRI. *Magn. Reson. Med.* 2017; 79:2685–2692.



- [44] Salimans T, Karpathy A, Chen X, Kingma DP. PixelCNN++: Improving the PixelCNN with Discretized Logistic Mixture Likelihood and Other Modifications. arXiv 2017; arXiv:1701.05517.
- [45] Rosenzweig S, Holme HCM, Uecker M. Simple auto-calibrated gradient delay estimation from few spokes using Radial Intersections (RING). *Magn. Reson. Med.* 2019; 81:1898–1906.
- [46] Hansen MS, Sørensen TS. Gadgetron: An open source framework for medical image reconstruction. *Magn. Reson. Med.* 2013; 69:1768–1776.
- [47] Xue H, Davies R, Hansen D, Tseng E, Fontana M, Moon JC, Kellman P. Gadgetron Inline AI: Effective Model inference on MR scanner. In: *Proc. Intl. Soc. Mag. Reson. Med.*, Montreal, 2019. p. 4837.
- [48] Diakite M, CampbellWashburn AE, Xue H. Integration of the BART Toolbox into Gadgetron Streaming Framework for Inline Cloud-Based Reconstruction. In: *Proc. Intl. Soc. Mag. Reson. Med.*, Paris, 2018. p. 2861.
- [49] Block KT, Sodickson DK. Yarra: An open software framework for clinical evaluation of reconstruction prototypes. In: *ISMRM Workshop on Data Sampling & Image Reconstruction*, Sedona, 2016.